

# Sub-6 nm Fully Ordered $L1_0$ -Pt–Ni–Co Nanoparticles Enhance Oxygen Reduction via Co Doping Induced Ferromagnetism Enhancement and Optimized Surface Strain

Tanyuan Wang, Jiashun Liang, Zhonglong Zhao, Shenzhou Li, Gang Lu, Zhengcai Xia, Chao Wang, Jiahuan Luo, Jiantao Han, Cheng Ma,\* Yunhui Huang,\* and Qing Li\*

Engineering the crystal structure of Pt–M (M = transition metal) nanoalloys to chemically ordered ones has drawn increasing attention in oxygen reduction reaction (ORR) electrocatalysis due to their high resistance against M etching in acid. Although Pt–Ni alloy nanoparticles (NPs) have demonstrated respectable initial ORR activity in acid, their stability remains a big challenge due to the fast etching of Ni. In this work, sub-6 nm monodisperse chemically ordered  $L1_0$ -Pt–Ni–Co NPs are synthesized for the first time by employing a bifunctional core/shell Pt/NiCoO<sub>x</sub> precursor, which could provide abundant O-vacancies for facilitated Pt/Ni/Co atom diffusion and prevent NP sintering during thermal annealing. Further, Co doping is found to remarkably enhance the ferromagnetism (room temperature coercivity reaching 2.1 kOe) and the consequent chemical ordering of  $L1_0$ -Pt–Ni NPs. As a result, the best-performing carbon supported  $L1_0$ -PtNi<sub>0.8</sub>Co<sub>0.2</sub> catalyst reveals a half-wave potential ( $E_{1/2}$ ) of 0.951 V versus reversible hydrogen electrode in 0.1 M HClO<sub>4</sub> with 23-times enhancement in mass activity over the commercial Pt/C catalyst along with much improved stability. Density functional theory (DFT) calculations suggest that the  $L1_0$ -PtNi<sub>0.8</sub>Co<sub>0.2</sub> core could tune the surface strain of the Pt shell toward optimized Pt–O binding energy and facilitated reaction rate, thereby improving the ORR electrocatalysis.


proton exchange membrane fuel cells (PEMFCs).<sup>[1–4]</sup> Pt nanoparticles (NPs) supported on carbon (Pt/C) is the state-of-the-art ORR catalyst equipped at the cathode of a PEMFC. However, the prohibitive cost and unsatisfactory activity/durability of the Pt/C catalyst, mainly caused by the Pt NP dissolution/migration in acidic environments, have been the greatest obstacle of the commercialization of PEMFCs. To this end, considerable research efforts have been devoted to developing advanced Pt-based ORR electrocatalysts with low Pt content, enhanced activity, and high stability.<sup>[5–12]</sup> During the last decade, alloying Pt with early transition metals (M) such as Fe, Co, Ni, and Cu with well-controlled size, shape, and composition represents the leading research activities in the community and dramatic enhancements in ORR activity and reduced usage of Pt have been achieved.<sup>[8,13–17]</sup> Specifically, theoretical calculations have indicated that the ORR activity improvement on such Pt–M catalysts can be attributed to the downshift of

The sluggish kinetics of oxygen reduction reaction (ORR) has been an enduring roadblock to the development of sustainable electrochemical energy conversion technologies, especially

d-band center and the optimized adsorption strength of oxygenated reaction intermediates (OH\*, O\*, OOH\*, etc.) compared to the Pt/C catalyst.<sup>[14,18]</sup> However, Pt–M alloy NPs usually

Prof. T. Wang, J. Liang, S. Li, Dr. J. Luo, Prof. J. Han, Prof. Y. Huang, Prof. Q. Li  
State Key Laboratory of Material Processing and Die and Mould Technology  
School of Materials Science and Engineering  
Huazhong University of Science and Technology  
Wuhan, Hubei 430074, China  
E-mail: huangyh@hust.edu.cn; qing\_li@hust.edu.cn

Dr. Z. Zhao, Prof. G. Lu  
Department of Physics and Astronomy  
California State University Northridge  
Northridge, CA 91330, USA

 The ORCID identification number(s) for the author(s) of this article can be found under <https://doi.org/10.1002/aenm.201803771>.

DOI: 10.1002/aenm.201803771

Prof. Z. Xia  
Wuhan National High Magnetic Field Center  
Huazhong University of Science and Technology  
Wuhan, Hubei 430074, China

Dr. C. Wang  
Department of Nuclear Science and Engineering  
Massachusetts Institute of Technology  
Cambridge, MA 02139, USA

Prof. C. Ma  
Division of Nanomaterials and Chemistry  
Hefei National Laboratory for Physical Sciences at the Microscale  
CAS Key Laboratory of Materials for Energy Conversion  
Department of Materials Science and Engineering  
University of Science and Technology of China  
Hefei, Anhui 230026, China  
E-mail: mach16@ustc.edu.cn

adopt a disordered face-centered cubic (fcc, A1 structure) solid-solution structure in which M and Pt are randomly distributed. When these Pt–M NPs are exposed to the corrosive conditions in acid-based PEMFCs, M is subject to fast etching that leaves a defective Pt surface with much low-coordinated Pt atoms, which leads to the structural and performance degradation.

Recently, it has been reported that the M stability in Pt–M alloy catalysts can be dramatically improved once the M and Pt are in a chemically ordered intermetallic structure (tetragonal  $L1_0$  or cubic  $L1_2$  structures).<sup>[11,19–21]</sup> Especially, for  $L1_0$ –PtM systems with Pt:M molar ratio of 1:1, the intermetallic structure would induce a strong 3d–5d orbital interaction between M and Pt along the crystallographic  $c$  direction, which does not exist in the fcc counterpart. Such strong Pt–M interaction would stabilize M more effectively in close-packed structures, leading to reduced etching and improved structural stability under acidic fuel cell conditions. Furthermore, theoretical calculations indicate that the surface Pt–O binding energetics could be optimized due to surface strains exerted by the intermetallic PtM core,<sup>[22–24]</sup> which essentially benefits the ORR activity of  $L1_0$ –Pt–M catalysts. For example, the fully ordered  $L1_0$ –FePt NPs demonstrate significantly improved ORR activity and durability in acid compared to the disordered A1–FePt.<sup>[19]</sup> Other intermetallic Pt–M systems including Pt–Co,<sup>[25,26]</sup> Pt–Cu,<sup>[27]</sup> Pt–Pb,<sup>[28]</sup> and Pt–Ga<sup>[29]</sup> have also demonstrated enhanced ORR activity and stability compared to their disordered counterparts. On the other hand, Pt–Ni alloys with controlled size and morphology are a group of well investigated ORR electrocatalysts with high activity,<sup>[17,30–32]</sup> as the (111) crystal facet of Pt<sub>3</sub>Ni is suggested to be one of the most active structures for ORR electrocatalysis.<sup>[33–35]</sup> Unfortunately, Pt–Ni catalysts also suffer from severe Ni etching in acid during ORR.<sup>[7,35,36]</sup> Intermetallic Pt–Ni nanostructures have been explored as ORR catalysts notwithstanding,<sup>[37,38]</sup> the crystal structure-catalytic performance correlations of Pt–Ni NPs are far less investigated compared to other magnetic Pt–M systems such as Pt–Fe and Pt–Co. It is primarily due to the fact that the reported intermetallic Pt–Ni catalysts generally show lower intrinsic ORR activity compared to that of disordered Pt<sub>3</sub>Ni alloys.<sup>[33,35,37]</sup> Meanwhile, disorder-order phase transformation is usually realized by high temperature annealing (>500 °C), which easily causes NP sintering and leads to the difficulty in preparing small-sized Pt–M NP catalysts (<6 nm) with high quality.<sup>[21,38]</sup> On the other hand, the commonly used spherical Pt–M alloy NP precursors (or Pt–M NPs coated with MgO/SiO<sub>2</sub> protective layers<sup>[19]</sup>) would greatly limit atom mobility during phase transformation. As a result, most of the reported intermetallic Pt–M systems are only partially ordered,<sup>[22,39]</sup> which essentially compromise the benefits of intermetallic structure on ORR catalysis.

Herein, monodisperse sub-6 nm fully ordered  $L1_0$ –PtNi (1:1 molar ratio) and  $L1_0$ –Pt–Ni–Co NP catalysts were successfully prepared by employing core/shell Pt/metal oxide precursors (e.g., NiO<sub>x</sub> and NiCoO<sub>x</sub>) for the first time. During A1– $L1_0$  phase transformation, the metal oxide shells could stabilize the NP against sintering and the in situ formed O vacancies could effectively promote the Pt/Ni diffusion. More importantly, Co doping into  $L1_0$ –PtNi is found to induce significant ferromagnetism enhancement and the resulted  $L1_0$ –ordering degree, which greatly improve their ORR activity and

durability in acid. The optimized Co incorporated  $L1_0$ –PtNi NPs ( $L1_0$ –PtNi<sub>0.8</sub>Co<sub>0.2</sub>) exhibit extraordinarily high ORR activity (23-times enhancement in mass activity at 0.9 V versus reversible hydrogen electrode (RHE) compared to the commercial Pt/C catalyst) and durability (stable after 10000 potential cycles in 0.1 M HClO<sub>4</sub>). X-ray adsorption spectra (XAS) indicate that the Pt in  $L1_0$ –PtNi<sub>0.8</sub>Co<sub>0.2</sub> is less oxidized with shorter Pt–Pt and Pt–Ni bonds compared to the A1 counterpart. Density functional theory (DFT) calculations suggest that the incorporation of Co in the  $L1_0$ –PtNi alloy core could optimize the surface strain and weaken the Pt–O binding energy ( $E_O$ ), leading to enhanced ORR kinetics.

To prepare sub-6 nm  $L1_0$ –Pt–Ni–Co NPs, ≈6 nm core/shell Pt/NiCoO<sub>x</sub> NPs were first synthesized via a facile one-pot method by the thermal decomposition of Pt(II) acetylacetonate (Pt(acac)<sub>3</sub>), Ni(acac)<sub>3</sub>, and Co(acac)<sub>3</sub> in the mixture of 1-octadecene and oleylamine (Figure 1a). During the synthesis, glucose and polyvinylpyrrolidone were employed as reductive and protective agents, respectively. A mild heating temperature (140 °C) was used to enable the growth of NiCoO<sub>x</sub> layers at the surface of Pt NPs.<sup>[40]</sup> The obtained Pt/NiCoO<sub>x</sub> NPs were then loaded on carbon black and annealed at 300 °C or 600 °C in forming gas (95/5 Ar/H<sub>2</sub>) to form A1- and  $L1_0$ –PtNi<sub>x</sub>Co<sub>1-x</sub> NPs (denoted as C-A1–PtNi<sub>x</sub>Co<sub>1-x</sub> and C- $L1_0$ –PtNi<sub>x</sub>Co<sub>1-x</sub>), respectively. During reductive thermal annealing, the NiCoO<sub>x</sub> layer could serve as a bifunctional component which not only offers large amounts of O-vacancies (by reducing NiCoO<sub>x</sub> to metallic Ni and Co) but also serves as a robust shield to prevent the NPs against sintering without the presence of additional oxide protections (e.g., MgO and SiO<sub>2</sub>). Compared to the commonly used Pt–M alloy NP precursors in which the atom mobility is strictly limited, the novel core/shell Pt/NiCoO<sub>x</sub> structure could create a 3D scaffold with abundant Ni/Co atoms and defects/vacancies surrounding Pt core during annealing, where the Pt/ Ni/Co diffusion during annealing could take place in a much facilitated way and eventually evolve into fully ordered  $L1_0$ –Pt–Ni–Co NPs. To investigate the Co doping effect on the ORR performance of  $L1_0$ –PtNi NPs, carbon supported ≈5 nm  $L1_0$ –PtNi,  $L1_0$ –PtNi<sub>0.9</sub>Co<sub>0.1</sub>,  $L1_0$ –PtNi<sub>0.8</sub>Co<sub>0.2</sub>,  $L1_0$ –PtNi<sub>0.6</sub>Co<sub>0.4</sub>,  $L1_0$ –PtNi<sub>0.4</sub>Co<sub>0.6</sub>,  $L1_0$ –PtNi<sub>0.2</sub>Co<sub>0.8</sub>, and  $L1_0$ –PtCo NPs are also prepared by tuning the added amounts of Ni/Co precursors (Figures S1 and S2, Supporting Information). The Pt/Ni/Co molar composition in the C- $L1_0$ –PtNi<sub>0.8</sub>Co<sub>0.2</sub> sample is measured to be 49/39/12, as determined by inductively coupled plasma atomic emission spectrometer (ICP-AES).

Figure 1b demonstrates the transmission electron microscopic (TEM) image of Pt/Ni<sub>0.8</sub>Co<sub>0.2</sub>O<sub>x</sub> NPs, which reveals an average size of  $6.1 \pm 0.4$  nm. High-resolution TEM (HRTEM) of Pt/Ni<sub>0.8</sub>Co<sub>0.2</sub>O<sub>x</sub> NPs shows that the core of the NP has higher contrast with an interplanar distance of ≈0.23 nm which corresponds to the (111) plane of fcc Pt, while the shell exhibits lower contrast with a lattice spacing of ≈0.24 nm, assignable to the (111) plane of bunsenite NiO (Figure 1c).<sup>[40]</sup> X-ray diffraction (XRD) pattern of the C–Pt/Ni<sub>0.8</sub>Co<sub>0.2</sub>O<sub>x</sub> sample (Figure S3, Supporting Information) verifies the existence of Pt and NiO peaks. The diffraction peaks of NiO are extremely weak, suggesting that the Ni<sub>0.8</sub>Co<sub>0.2</sub>O<sub>x</sub> shell is poorly crystallized. To further confirm the core/shell structure of the Pt/Ni<sub>0.8</sub>Co<sub>0.2</sub>O<sub>x</sub> NPs, linear-scan energy dispersive X-ray (EDX) spectroscopy is

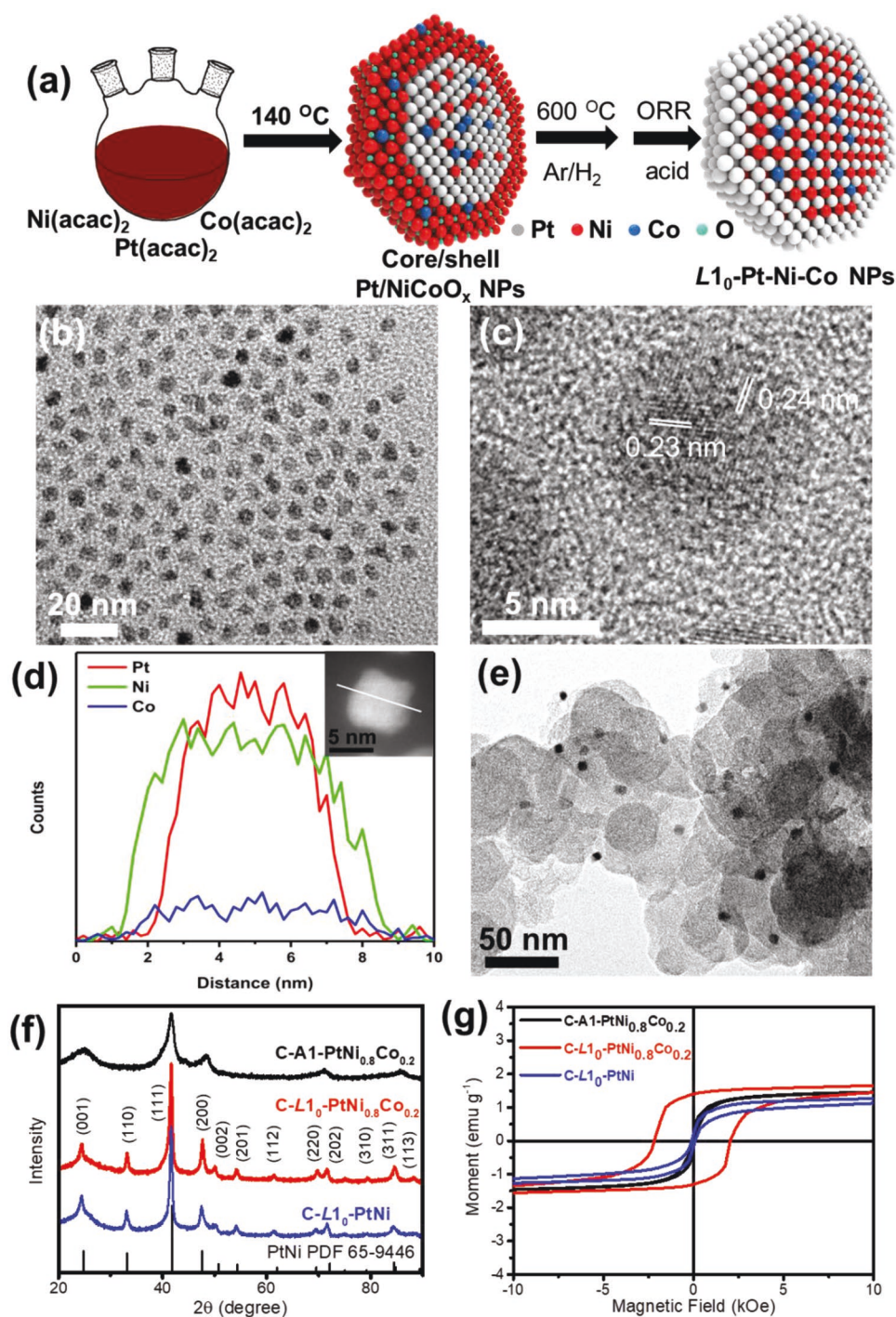


**Figure 1.** a) Fabrication of  $L1_0$ -Pt-Ni-Co NPs with Pt-rich shell. b) TEM and c) HRTEM images of core/shell Pt/ $Ni_{0.8}Co_{0.2}O_x$  NPs. d) EDX line-scan profile of a representative core/shell Pt/ $NiCoO_x$  NP. e) TEM image of C- $L1_0$ -Pt $Ni_{0.8}Co_{0.2}$  NPs. f) XRD patterns and g) Hysteresis loops of C-A1-Pt $Ni_{0.8}Co_{0.2}$ , C- $L1_0$ -Pt $Ni_{0.8}Co_{0.2}$ , and C- $L1_0$ -PtNi NPs.

conducted. As shown in Figure 1d, Ni-Co shell with a thickness of  $\approx 1$  nm can be detected for this sample. After loading on carbon and thermal annealing, the obtained both A1- (Figure S4, Supporting Information) and  $L1_0$ -Pt-Ni-Co NPs (Figure 1e; Figure S2, Supporting Information) could keep their sizes uniform and no NP agglomeration is observed. Specifically,

the  $L1_0$ -Pt $Ni_{0.8}Co_{0.2}$  NPs show an average size of  $5.0 \pm 0.3$  nm (Figure 1e). As NPs are thermodynamically inclined to aggregate/sinter during high temperature annealing without protecting template,<sup>[21,40]</sup> the presence of  $NiCoO_x$  shells could indeed serve as an effective protection layer to prevent the NP aggregation. XRD patterns of the synthesized NPs are collected



to demonstrate their crystal structures (Figure 1f). Obviously, the C-A1-PtNi<sub>0.8</sub>Co<sub>0.2</sub> and C-A1-PtNi (Figure S5, Supporting Information) samples display diffraction peaks close to that of common fcc Pt-based alloys, indicating that annealing at 300 °C could only initiate the alloying process of Pt core and NiCoO<sub>x</sub> shell into a chemically disordered Pt–Ni–Co alloy. When annealing at 600 °C, the C-L1<sub>0</sub>-PtNi<sub>0.8</sub>Co<sub>0.2</sub> sample exhibits not only characteristic (001) and (110) peaks for the tetragonal PtNi (PDF# 65-9446) but also other weak intermetallic peaks including (002), (201), (112), (220), (310), and (113), pointing to the formation of the L1<sub>0</sub>-ordering structures. The intensity ratio of (110)/(111) peaks, which reflects the degree of ordering,<sup>[41]</sup> is measured to be 0.244 for C-L1<sub>0</sub>-PtNi<sub>0.8</sub>Co<sub>0.2</sub> and close to that of bulk L1<sub>0</sub>-PtNi (0.285), indicating the fully ordered crystal structure of C-L1<sub>0</sub>-PtNi<sub>0.8</sub>Co<sub>0.2</sub>. In addition, the diffraction peaks of C-L1<sub>0</sub>-PtNi and other C-L1<sub>0</sub>-PtNi<sub>x</sub>Co<sub>1-x</sub> samples (Figure S6, Supporting Information) also match well with the standard diffraction patterns of tetragonal PtNi.

The A1-L1<sub>0</sub> phase transformation of the C-PtNi<sub>0.8</sub>Co<sub>0.2</sub> sample is further supported by the magnetic measurements. Unlike A1-Pt–Ni–Co NPs with disordered structure which exhibit superparamagnetic behavior at room temperature, the L1<sub>0</sub>-PtNi<sub>0.8</sub>Co<sub>0.2</sub> NPs, due to the strong *d* electron interaction between Pt and Ni/Co in the chemically ordered structure, are strongly ferromagnetic (Figure 1g). Although L1<sub>0</sub>-PtNi NPs showing an inherently low coercivity (*H<sub>c</sub>*) of 2.1 Oe,<sup>[42]</sup> the incorporation of Co into L1<sub>0</sub>-PtNi NPs is found to remarkably enhance their ferromagnetism and chemical ordering.<sup>[43,44]</sup> Previous study has demonstrated that 80% substitution of Ni for Co in epitaxial L1<sub>0</sub>-PtCo film is able to promote atomic diffusivity during phase transformation, resulting in a much increased *H<sub>c</sub>* of ≈2.0 kOe.<sup>[44]</sup> In our system, the developed 5 nm L1<sub>0</sub>-PtNi<sub>0.8</sub>Co<sub>0.2</sub> NPs have a single-phase loop and the *H<sub>c</sub>* reaches ≈2.1 kOe at room temperature. Importantly, this is a very large ferromagnetic *H<sub>c</sub>* value for the sub-6 nm NPs, even superior to that measured with L1<sub>0</sub>-Pt–Ni–Co films,<sup>[42–44]</sup> manifesting the extremely high L1<sub>0</sub>-ordering degree in our sample. Thanks to the unique Pt/NiCoO<sub>x</sub> core/shell configuration, the local atomic arrangements and lattice positions of Pt/Ni/Co atoms could be more easily regulated during thermal annealing and finally evolve into the “fully ordered” crystal structure. X-ray photoelectron spectroscopy is used to characterize the bonding configuration of A1- and L1<sub>0</sub>-PtNi<sub>0.8</sub>Co<sub>0.2</sub> samples (Figure S7, Supporting Information). Both samples demonstrate a Pt 4f<sub>7/2</sub> binding energy of 71.5 eV, corresponding to the metallic Pt. However, a negative shift of Ni 2p<sub>5/2</sub> peak from 856.1 to 855.2 eV can be observed for L1<sub>0</sub>-PtNi<sub>0.8</sub>Co<sub>0.2</sub> after phase transformation, likely due to the increased oxidation resistance of intermetallic PtNi<sub>0.8</sub>Co<sub>0.2</sub> NPs.<sup>[37]</sup>

The electrochemical properties of C-A1-PtNi<sub>0.8</sub>Co<sub>0.2</sub>, C-L1<sub>0</sub>-PtNi<sub>0.8</sub>Co<sub>0.2</sub>, and commercial Pt/C catalysts are investigated by cyclic voltammetry (CV) in N<sub>2</sub>-saturated 0.1 M HClO<sub>4</sub> electrolyte (Figure 2a). Typical hydrogen underpotential (*H<sub>upd</sub>*) absorption and desorption peaks can be observed for these catalysts. The electrochemical surface area (ECSA) of these samples can be calculated by integrating the *H<sub>upd</sub>* areas and normalized to the mass loading of Pt (see the Supporting Information for details). The ECSA of C-A1-PtNi<sub>0.8</sub>Co<sub>0.2</sub> and C-L1<sub>0</sub>-PtNi<sub>0.8</sub>Co<sub>0.2</sub> are measured to be 57 and 52 m<sup>2</sup> g<sub>Pt</sub><sup>−1</sup> respectively, comparable

to that of commercial Pt/C. The ORR activity of the developed C-L1<sub>0</sub>-Pt–Ni–Co and commercial Pt/C catalysts are evaluated by rotating disk electrode polarization curves in O<sub>2</sub>-saturated 0.1 M HClO<sub>4</sub> (Figure 2b). Unsurprisingly, the C-A1-PtNi<sub>0.8</sub>Co<sub>0.2</sub> catalyst exhibits higher ORR activity with more positive onset potential and half-wave potential (*E*<sub>1/2</sub>) compared to that of the commercial Pt/C (*E*<sub>1/2</sub> 0.912 V vs 0.877 V), demonstrating the promotional effect of alloying Pt with Ni and Co. Importantly, further transforming A1 to L1<sub>0</sub> structure leads to a dramatic enhancement in *E*<sub>1/2</sub> as positive as 0.951 V versus RHE, which represents one of the most positive values for intermetallic Pt–M catalysts.<sup>[11,20–22,27]</sup> The remarkable ORR activity of the developed L1<sub>0</sub>-PtNi<sub>0.8</sub>Co<sub>0.2</sub> NPs could be attributed to their extremely high crystal ordering structure and the optimized electronic structure induced by Co doping. Analysis of Tafel plots indicate that all the samples display Tafel slopes of ≈60 mV dec<sup>−1</sup> at low overpotential region and ≈120 mV dec<sup>−1</sup> at higher one (Figure S8, Supporting Information), suggesting identical ORR rate-determining steps for all three catalysts.<sup>[19]</sup> The mass and specific activities of the studied catalysts at 0.9 V are calculated and listed in Figure 2c,d, respectively. The C-L1<sub>0</sub>-PtNi<sub>0.8</sub>Co<sub>0.2</sub> catalyst shows high mass and specific activities of 2.28 A mg<sub>Pt</sub><sup>−1</sup> and 4.38 mA cm<sup>−2</sup>, which reveal 23- and 19-times improvement compared to that of the commercial Pt/C (0.10 A mg<sub>Pt</sub><sup>−1</sup> and 0.23 mA cm<sup>−2</sup>), respectively. Importantly, the initial ORR activity of the C-L1<sub>0</sub>-PtNi<sub>0.8</sub>Co<sub>0.2</sub> catalyst is comparable to that of the best reported PtNi-based systems and other intermetallic ORR electrocatalysts (Table 1). To elucidate the effect of Co doping, the ORR performance of other intermetallic C-L1<sub>0</sub>-Pt–Ni–Co NPs as well as C-L1<sub>0</sub>-PtNi and C-L1<sub>0</sub>-PtCo are also evaluated (Figure 2e; Figure S9, Supporting Information). Among all the studied catalysts, C-L1<sub>0</sub>-PtNi displays the most negative *E*<sub>1/2</sub> (0.899 V), indicating that L1<sub>0</sub>-PtNi is not intrinsically active for ORR. Partially replacing Ni by Co could significantly improve the *E*<sub>1/2</sub> of C-L1<sub>0</sub>-Pt–Ni–Co NPs and the optimal *E*<sub>1/2</sub> is achieved at the Ni/Co ratio of 8/2. Further decreasing Ni/Co ratios to 6/4, 4/6, and 2/8 leads to insignificant influence on *E*<sub>1/2</sub> (0.92–0.93 V), which are close to that on C-L1<sub>0</sub>-PtCo NPs. Among the L1<sub>0</sub>-Pt–Ni–Co NPs, L1<sub>0</sub>-PtNi<sub>0.8</sub>Co<sub>0.2</sub> may show the optimized *E*<sub>0</sub> due to the downshift of d-band center that originates from the coupling of Pt, Ni, and Co with a proper ratio, thus demonstrates the best ORR performance.

The stability of the developed L1<sub>0</sub>-Pt–Ni–Co catalysts is evaluated by accelerated durability test in O<sub>2</sub>-saturated 0.1 M HClO<sub>4</sub>. After potential cycling from 0.6 to 1.0 V for 5000 and 10 000 cycles, the C-L1<sub>0</sub>-PtNi<sub>0.8</sub>Co<sub>0.2</sub> catalyst demonstrates almost unchanged polarization curve (Figure 2f; Figure S10, Supporting Information), while a negative shift of ≈59 mV in *E*<sub>1/2</sub> can be detected for the A1 counterpart after only 5000 cycles (Figure S11, Supporting Information). Furthermore, the Pt/Ni/Co ratio for C-A1-PtNi<sub>0.8</sub>Co<sub>0.2</sub> changes from 48/41/11 to 71/22/7 after stability test as measured by ICP-AES, while for C-L1<sub>0</sub>-PtNi<sub>0.8</sub>Co<sub>0.2</sub> it only changes slightly from 49/39/12 to 55/35/10. These results demonstrate the promotional effect of fully ordered L1<sub>0</sub>-PtNi<sub>0.8</sub>Co<sub>0.2</sub> catalyst on suppressing the dissolution of Ni in acid and thus improving the structural stability during ORR electrocatalysis. Figure 3a demonstrates the atomic-resolution high-angle annular dark field scanning transmission

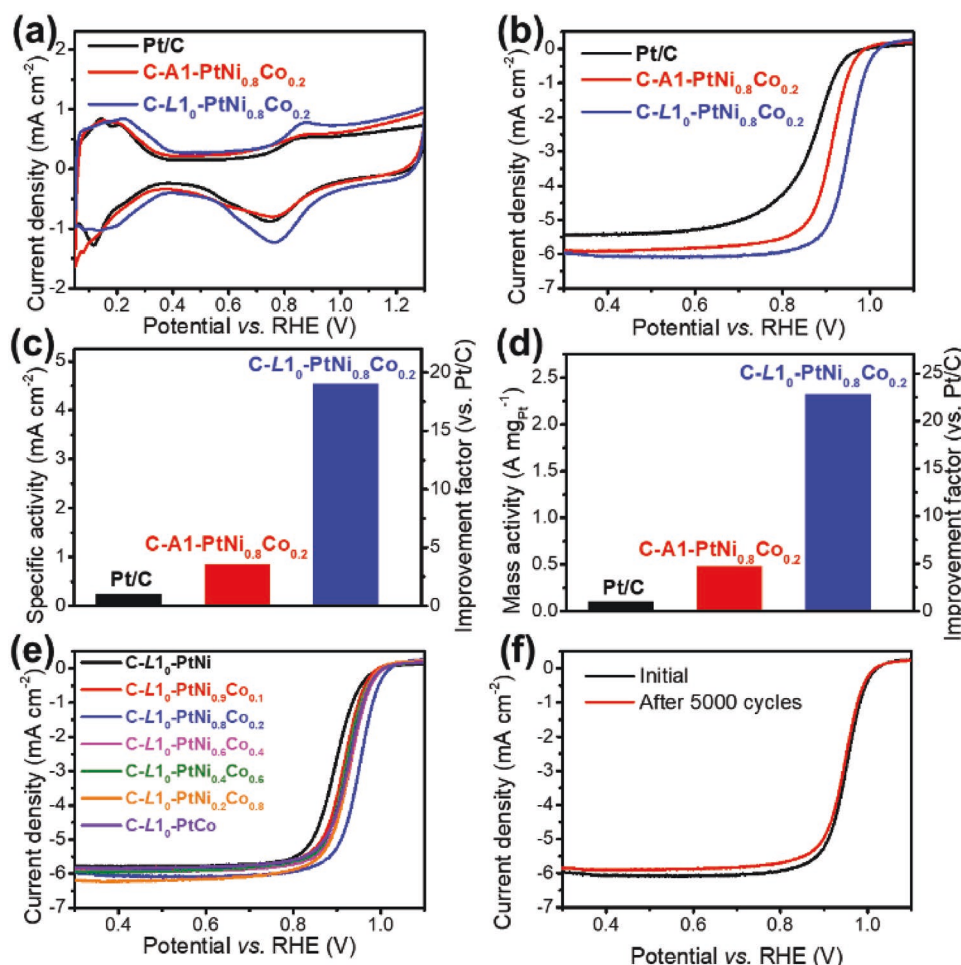


**Figure 2.** a) CV curves of commercial Pt/C, C-A1-PtNi<sub>0.8</sub>Co<sub>0.2</sub>, and C-L1<sub>0</sub>-PtNi<sub>0.8</sub>Co<sub>0.2</sub> in N<sub>2</sub>-saturated 0.1 M HClO<sub>4</sub> with a scan rate of 50 mV s<sup>-1</sup>. b) LSV curves of commercial Pt/C, C-A1-PtNi<sub>0.8</sub>Co<sub>0.2</sub>, and C-L1<sub>0</sub>-PtNi<sub>0.8</sub>Co<sub>0.2</sub> in O<sub>2</sub>-saturated 0.1 M HClO<sub>4</sub> at a rotation speed of 1600 rpm with a scan rate of 10 mV s<sup>-1</sup>. c) Mass activities of different catalysts at 0.9 V. d) Specific activities of different catalysts at 0.9 V. e) LSV curves of different C-L1<sub>0</sub>-PtNi<sub>0.8</sub>Co<sub>0.2</sub> NPs in O<sub>2</sub>-saturated 0.1 M HClO<sub>4</sub> at a rotation speed of 1600 rpm with a scan rate of 10 mV s<sup>-1</sup>. f) LSV curves of the C-L1<sub>0</sub>-PtNi<sub>0.8</sub>Co<sub>0.2</sub> catalyst before and after stability test.

electron microscopic (HAADF-STEM) image of a representative L1<sub>0</sub>-PtNi<sub>0.8</sub>Co<sub>0.2</sub> NP after stability test. The L1<sub>0</sub>-ordering structure is clearly indicated by the alternative Z-contrast stripes in the particle. Specifically, the alternate high (Pt) and low (Ni/Co) Z-contrast columns confirm the ordered arrangement of Pt and Ni/Co within the NP. Figure 3b–g shows the EDX linear scan and elemental mappings of a representative L1<sub>0</sub>-PtNi<sub>0.8</sub>Co<sub>0.2</sub> NP. Pt, Ni, and Co could all be clearly detected in the NP. Noteworthy, a thin Pt layer of ≈0.5 nm (Pt-skin) is observed due to the surface dealloying in acid (Figure 3c), which proves the formation of core/shell Pt–Ni–Co/Pt structure with ordered PtNi<sub>0.8</sub>Co<sub>0.2</sub> core and ≈2 atomic layers of Pt shell.<sup>[19,21]</sup> To elucidate the formation mechanism of Pt-skin, the structure and elemental distribution of the as-synthesized L1<sub>0</sub>-PtNi<sub>0.8</sub>Co<sub>0.2</sub> NPs are characterized by HRTEM and EDX. As shown in Figure S12a–e of the Supporting Information, ≈5 nm well-crystallized NP can be observed and Pt, Ni, and Co are uniformly distributed throughout the NP. Importantly, both Pt and Ni can be detected on the surface of the NP before electrochemical tests (Figure S12f,g, Supporting Information), indicating that the Pt-skin of the NP should be formed during the ORR

measurements. The formation of Pt-skin is commonly reported in the Pt–M (M = Fe, Co, Ni, Cu, etc.) alloy systems.<sup>[21,27,48]</sup> In acidic electrolyte, Ni and Co on the NP surface are more easily to be oxidized and dissolved compared to Pt, resulting in the formation of Pt-rich layer on the NP surface. The strong Pt(5d)–Ni/Co(3d) coupling<sup>[48]</sup> in L1<sub>0</sub>-PtNi<sub>0.8</sub>Co<sub>0.2</sub> could prevent the further oxidation of Ni and Co in the core of the NPs. The formation Pt-skin structure is further certified by CO stripping measurement (Figure S13, Supporting Information). The C-L1<sub>0</sub>-PtNi<sub>0.8</sub>Co<sub>0.2</sub> catalyst after stability test demonstrates a sharper CO oxidation peak compared to as-synthesized one with a positive shift from 0.79 to 0.82 V, suggesting the formation of Pt layers on the surface of L1<sub>0</sub>-PtNi<sub>0.8</sub>Co<sub>0.2</sub> NPs.<sup>[48]</sup> The shoulder peak can be probably attributed to the oxidation of CO on the low coordination sites.<sup>[52]</sup> To better illustrate the structural stability of C-L1<sub>0</sub>-PtNi<sub>0.8</sub>Co<sub>0.2</sub> during ORR test, HRTEM and EDX profiles of the A1-PtNi<sub>0.8</sub>Co<sub>0.2</sub> NPs are carried out. As shown in Figure S14a, A1-PtNi<sub>0.8</sub>Co<sub>0.2</sub> NPs tend to aggregate after stability test. Even though Pt, Ni, and Co are still present in the NP (Figure S14b–e, Supporting Information), the Pt/Ni/Co ratio changes from 5/4/1 to ≈6/3/1, attesting to the

**Table 1.** A summary of ORR performance of PtM-based nanomaterials in recent studies.

Catalyst	$E_{1/2}$ [V]	Specific activity at 0.90 V [ $\text{mA cm}^{-2}$ ]	Mass activity at 0.90 V [ $\text{A mg}_{\text{Pt}}^{-1}$ ]	Ref.
Porous Pt <sub>3</sub> Ni nanocrystals/C	0.909	1.006	0.757	[35]
Pt-skin Pt <sub>3</sub> Ni/C	0.905	–	0.69	[45]
9 nm Pt <sub>2.5</sub> Ni octahedra/C	<0.93	3.4 (at 0.93 V)	3.3	[17]
Mo-doped Pt <sub>3</sub> Ni octahedra/C	–	10.3	6.98	[33]
9.5 nm PtNi octahedra/C	–	3.14	1.45	[32]
PtNi core-shell NP/C	0.905	1.65	0.86	[31]
Ga-doped Pt-Ni octahedra/C	–	2.53	1.24	[46]
PtNi nano-octahedra/C	0.92	3.8	1.65	[36]
Fully ordered L1 <sub>0</sub> -FePt/C	0.958	3.16	0.69	[19]
8.9 nm L1 <sub>0</sub> -CoPt/C	0.967	8.26	2.26	[25]
3.6 nm L1 <sub>0</sub> -FePt/C	0.893	0.37	1.1	[47]
8 nm L1 <sub>0</sub> -FePt/Pt/C	0.945	–	0.7	[48]
PtPb/Pt core/shell nanoplate/C	–	7.8	4.3	[28]
Ordered Fe <sub>3</sub> Pt/Ti <sub>0.5</sub> Cr <sub>0.5</sub> N	0.92	1.28	0.57	[49]
3 nm AuCu <sub>3</sub> /C (0.1 M KOH)	0.82	–	0.523 (at 0.8 V)	[50]
L1 <sub>2</sub> -Cu <sub>3</sub> Pt/C	0.872	1.73	0.64	[51]
Ordered Pt <sub>3</sub> Co/C	0.945	1.1	0.52	[21]
C-L1 <sub>0</sub> -PtNi <sub>0.8</sub> Co <sub>0.2</sub>	0.951	4.38	2.28	This work

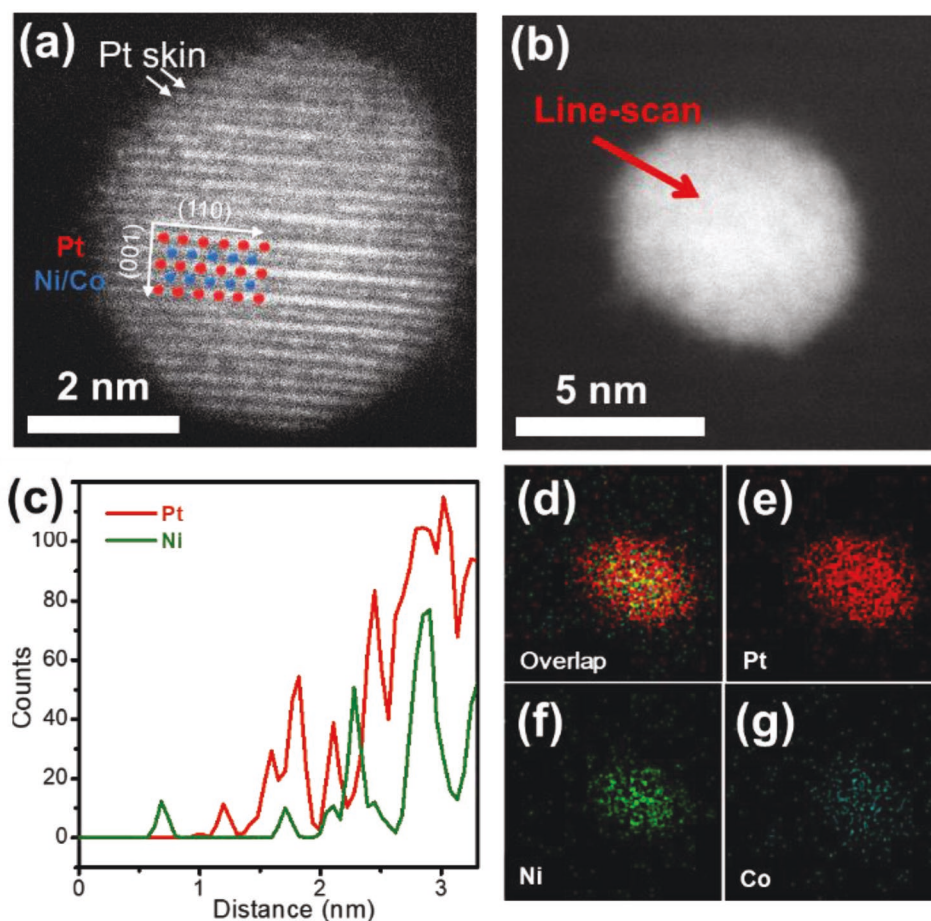


**Figure 3.** a,b) HAADF-STEM images, c) EDX line-scan profiles, and d–g) EDX mappings of a L1<sub>0</sub>-PtNi<sub>0.8</sub>Co<sub>0.2</sub> NP after 5000 potential cycles.



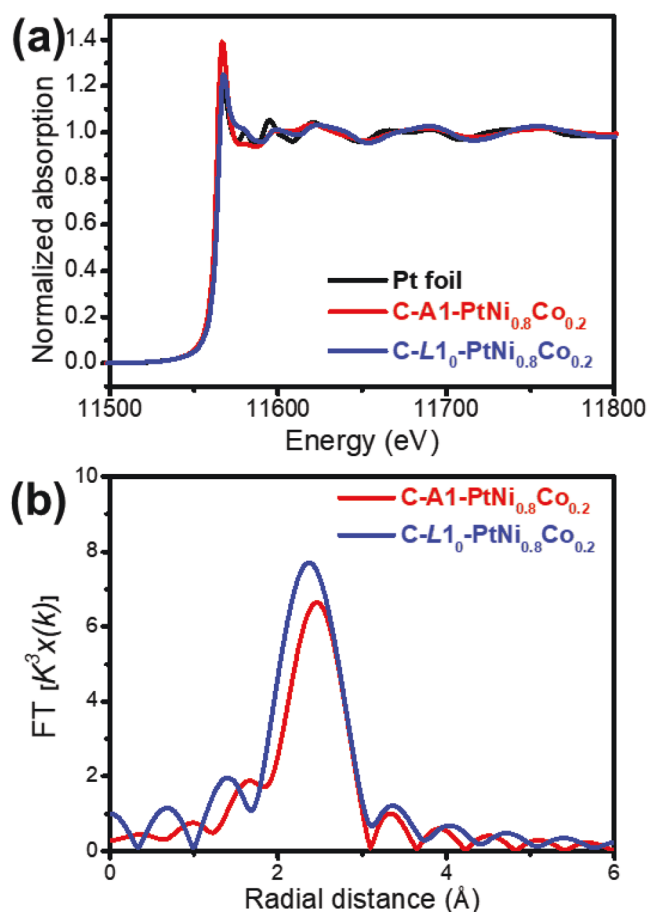


**Figure 4.** a) Pt L<sub>3</sub> XANES spectra of C-A1-PtNi<sub>0.8</sub>Co<sub>0.2</sub>, C-L1<sub>0</sub>-PtNi<sub>0.8</sub>Co<sub>0.2</sub>, and Pt foil samples. b) Pt L<sub>3</sub>k<sup>3</sup>-weighted FT-EXAFS spectra of C-A1-PtNi<sub>0.8</sub>Co<sub>0.2</sub> and C-L1<sub>0</sub>-PtNi<sub>0.8</sub>Co<sub>0.2</sub>.

loss of Ni during stability test. For L1<sub>0</sub>-PtNi<sub>0.8</sub>Co<sub>0.2</sub>, its Pt/Ni/Co ratio keeps 5/4/1 after stability test according to EDX characterization, certifying the dissolution-resistant nature of ordered state. EDX linear scan further proves the improved chemical stability of L1<sub>0</sub>-PtNi<sub>0.8</sub>Co<sub>0.2</sub>. A Pt layer of ≈1 nm can be observed for A1-PtNi<sub>0.8</sub>Co<sub>0.2</sub> after 5000 potential cycles (Figure S14f,g, Supporting Information), while the Pt-skin is only 0.5 nm for L1<sub>0</sub>-PtNi<sub>0.8</sub>Co<sub>0.2</sub> (Figure 3c), implying the enhanced stability of the ordered core. XAS measurements are carried out to further understand the valence state and atomic structure of A1- and L1<sub>0</sub>-PtNi<sub>0.8</sub>Co<sub>0.2</sub> NPs. The white line peak (the main peak just after the edge) intensity in the X-ray adsorption near-edge structure (XANES) spectra at Pt L<sub>3</sub>-edge is associated with the degree of oxidation as well as electronic transition from the 2p<sup>3/2</sup> orbital to the unoccupied 5d orbitals for Pt.<sup>[46,53]</sup> As shown in Figure 4a, the A1-PtNi<sub>0.8</sub>Co<sub>0.2</sub> sample demonstrates the most intense white line peak, while that of L1<sub>0</sub>-PtNi<sub>0.8</sub>Co<sub>0.2</sub> is much lower and very close to that of the metallic Pt foil, attesting the less-oxidized status of Pt in L1<sub>0</sub>-PtNi<sub>0.8</sub>Co<sub>0.2</sub> compared to the disordered one. As the oxidized Pt is less active than metallic Pt in ORR electrocatalysis,<sup>[54]</sup> the oxidation resistant L1<sub>0</sub>-PtNi<sub>0.8</sub>Co<sub>0.2</sub> catalyst would definitely benefit the ORR performance. X-ray absorption fine structure (EXAFS) spectra of A1- and L1<sub>0</sub>-PtNi<sub>0.8</sub>Co<sub>0.2</sub> samples (Figure 4b; Figure S15,

Supporting Information) suggest that the average lengths of Pt–Pt and Pt–Ni bonds slightly decrease after the phase transformation due to the significant change in crystal structure. Specifically, the Pt–Pt bond length (2.748 Å for C-A1-PtNi<sub>0.8</sub>Co<sub>0.2</sub> and 2.695 Å for C-L1<sub>0</sub>-PtNi<sub>0.8</sub>Co<sub>0.2</sub>, Table S1, Supporting Information) is shorter than that of the bulk Pt (2.775 Å) due to the incorporation of smaller Ni/Co atoms into the crystal structure. Noteworthy, such decrease in Pt–Pt bond length could induce a compressive strain over the Pt surface, which has been demonstrated to be beneficial for the ORR performance.<sup>[55,56]</sup>

DFT calculations are performed to provide insights into the origin of the enhanced ORR performance on the L1<sub>0</sub>-PtNi<sub>0.8</sub>Co<sub>0.2</sub> catalyst. To this end, we focus on the oxygen adsorption energy ( $E_O$ ) which has been widely used as a descriptor of ORR activity.<sup>[57,58]</sup> Since there is an optimal  $E_O$  value under which the ORR activity reaches the maximum,<sup>[58]</sup> here we use  $\Delta E_O$  to represent the difference of a given  $E_O$  value relative to the optimal reference. A slab model shown schematically in Figure 5a is employed to calculate  $\Delta E_O$  on

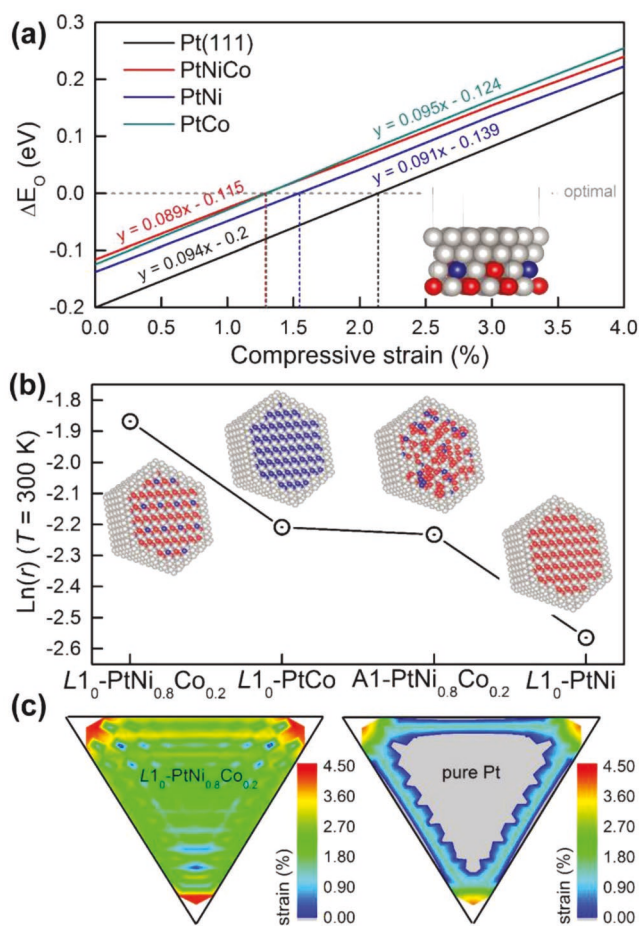


**Figure 5.** a)  $\Delta E_O$  as a function of compressive strain on the (111) surfaces of Pt, L1<sub>0</sub>-PtNi<sub>0.8</sub>Co<sub>0.2</sub>/Pt, L1<sub>0</sub>-PtNi/Pt, and L1<sub>0</sub>-PtCo/Pt. The optimal  $E_O$  is set to 0. The slab model of the surfaces is shown as inset. Gray, red, and blue spheres represent Pt, Ni, and Co atoms, respectively. b) The logarithm of the estimated ORR reaction rate on the core/shell NPs. The atomic structures of the NPs are shown in the insets. c) The color-coded strain distribution on the (111) surface of L1<sub>0</sub>-PtNi<sub>0.8</sub>Co<sub>0.2</sub> and pure Pt NPs. The gray area represents negative (or tensile) strain distribution.

(111) surfaces of pure Pt, core/shell  $L1_0$ -PtNi/Pt,  $L1_0$ -PtCo/Pt, and  $L1_0$ -PtNi<sub>0.8</sub>Co<sub>0.2</sub>/Pt (with 2 Pt atomic layers) under a biaxial compression up to 4%. Linear relationships between  $\Delta E_O$  and the compression are observed with an optimal compression of 2.1%, 1.53%, 1.31%, and 1.29% identified for Pt,  $L1_0$ -PtNi/Pt,  $L1_0$ -PtCo/Pt, and  $L1_0$ -PtNi<sub>0.8</sub>Co<sub>0.2</sub>/Pt, respectively. The surface strain distribution on  $L1_0$ -PtNi<sub>0.8</sub>Co<sub>0.2</sub>/Pt,  $L1_0$ -PtCo/Pt,  $L1_0$ -PtNi/Pt, A1-PtNi<sub>0.8</sub>Co<sub>0.2</sub>/Pt as well pure Pt NPs are also calculated using molecular mechanics method.<sup>[59]</sup> We model each NP with a truncated octahedron which has a diameter of  $\approx 5$  nm and a Pt shell of 2-atom-layer thickness shown in Figure 5b. Owing to the lattice mismatch between the alloy core and the Pt-shell, significant compression is developed on the (111) facets of Pt–Ni–Co NP (Figure 5c; Figure S16, Supporting Information). This is in a sharp contrast to the strain distribution on the pure Pt NP, which is dominated by tensile strains (gray area in Figure 5c) with smaller compressions at its edges and corners. Thus, the  $L1_0$ -PtNi<sub>0.8</sub>Co<sub>0.2</sub>/Pt core/shell structure is expected to be more active toward ORR than the pure Pt NP due to the strain effect. To be more quantitative, the overall ORR reaction rate ( $r$ ) on each NP is calculated using a well-established microkinetic model<sup>[60,61]</sup> and the results are displayed in Figure 5b. The estimated ORR reaction rates are in the order of  $L1_0$ -PtNi<sub>0.8</sub>Co<sub>0.2</sub> >  $L1_0$ -PtCo  $\approx$  A1-PtNi<sub>0.8</sub>Co<sub>0.2</sub> >  $L1_0$ -PtNi, which is perfectly consistent with the experimental trend. Overall, the enhanced ORR activity on  $L1_0$ -PtNi<sub>0.8</sub>Co<sub>0.2</sub> NP can be attributed to the synergy between the surface strain and ligand effects.

In conclusion, we report a facile and self-templated method to prepare monodisperse sub-6 nm  $L1_0$ -ordering Pt–Ni–Co NPs with extremely high ordering degree as ORR catalysts for the first time. The use of core/shell Pt/NiCoO<sub>x</sub> precursor is able to facilitate the kinetics of atom diffusion and prevent NP against sintering during annealing. Besides, Co doping could further enhance the ferromagnetism and the consequent chemical ordering of PtNi NPs. The optimized  $L1_0$ -PtNi<sub>0.8</sub>Co<sub>0.2</sub> NPs show enhanced ORR activity and stability compared with the disordered counterpart and commercial Pt/C, with mass activity (2.28 A mg<sub>Pt</sub><sup>−1</sup> at 0.9 V vs RHE) surpassing that of Pt/C by a 23-fold improvement. XAS reveals the Pt in  $L1_0$ -PtNi<sub>0.8</sub>Co<sub>0.2</sub> is less oxidized with shorter Pt–Pt bonds compared to the A1 counterpart. DFT simulations indicate that the compressive surface strain induced by  $L1_0$ -Pt–Ni–Co core results in an optimized  $E_O$  and ORR rate. This work not only demonstrates a novel strategy for the preparation of highly ordered intermetallic NPs and can be extended to other binary or ternary alloy catalysts for electrocatalysis enhancement.

## Supporting Information

Supporting Information is available from the Wiley Online Library or from the author.

## Acknowledgements

T.W. and J.L. contributed equally to this work. This work was financial supported by the National Natural Science Foundation of China (21603078, 21705052, 51602223, and 21801005) and the National Materials Genome Project (2016YFB0700600). The work at California

State University Northridge was supported by NSF-PREM program (DMR-1828019). The authors thank the Analytical and Testing Center of Huazhong University of Science and Technology (HUST) for carrying out the TEM and XRD measurements.

## Conflict of Interest

The authors declare no conflict of interest.

## Keywords

electrocatalysis, fuel cells, nanoparticles, oxygen reduction, phase transformation

Received: December 5, 2018

Revised: February 1, 2019

Published online:

- [1] A. S. Arico, P. Bruce, B. Scrosati, J. M. Tarascon, W. Van Schalkwijk, *Nat. Mater.* **2005**, *4*, 366.
- [2] Z. Miao, X. Wang, M. Tsai, Q. Jin, J. Liang, F. Ma, T. Wang, S. Zheng, B.-J. Hwang, Y. Huang, S. Guo, Q. Li, *Adv. Energy Mater.* **2018**, *8*, 1801226.
- [3] Y. Liang, Y. Li, H. Wang, J. Zhou, J. Wang, T. Regier, H. Dai, *Nat. Mater.* **2011**, *10*, 780.
- [4] Q. Li, N. Mahmood, J. Zhu, Y. Hou, S. Sun, *Nano Today* **2014**, *9*, 668.
- [5] Z. Xia, L. An, P. Chen, D. Xia, *Adv. Energy Mater.* **2016**, *6*, 1600458.
- [6] Q. Li, S. Sun, *Nano Energy* **2016**, *29*, 178.
- [7] C. Chen, Y. Kang, Z. Huo, Z. Zhu, W. Huang, H. Xin, J. D. Snyder, D. Li, J. A. Herron, M. Mavrikakis, M. Chi, K. L. More, Y. Li, N. M. Markovic, G. A. Somorjai, P. Yang, V. R. Stamenkovic, *Science* **2014**, *343*, 1339.
- [8] L. Zhang, L. T. Roling, X. Wang, M. Vara, M. Chi, J. Liu, S. I. Choi, J. Park, J. A. Herron, Z. Xie, M. Mavrikakis, Y. Xia, *Science* **2015**, *349*, 412.
- [9] Q. Li, P. Xu, B. Zhang, G. Wu, H. Zhao, E. Fu, H.-L. Wang, *Nanoscale* **2013**, *5*, 7397.
- [10] Z. Niu, N. Becknell, Y. Yu, D. Kim, C. Chen, N. Kornienko, G. A. Somorjai, P. Yang, *Nat. Mater.* **2016**, *15*, 1188.
- [11] B. Lim, M. Jiang, P. H. Camargo, E. C. Cho, J. Tao, X. Lu, Y. Zhu, Y. Xia, *Science* **2009**, *324*, 1302.
- [12] D. Wang, Y. Li, *Adv. Mater.* **2011**, *23*, 1044.
- [13] C. Wang, D. van der Vliet, K. L. More, N. J. Zaluzec, S. Peng, S. Sun, H. Daimon, G. Wang, J. Greeley, J. Pearson, A. P. Paulikas, G. Karapetrov, D. Strmcnik, N. M. Markovic, V. R. Stamenkovic, *Nano Lett.* **2011**, *11*, 919.
- [14] V. R. Stamenkovic, B. S. Mun, M. Arenz, K. J. J. Mayrhofer, C. A. Lucas, G. F. Wang, P. N. Ross, N. M. Markovic, *Nat. Mater.* **2007**, *6*, 241.
- [15] W. Wang, B. Lei, S. J. Guo, *Adv. Energy Mater.* **2016**, *6*, 1600236.
- [16] M. K. Carpenter, T. E. Moylan, R. S. Kukreja, M. H. Atwan, M. M. Tessema, *J. Am. Chem. Soc.* **2012**, *134*, 8535.
- [17] S. I. Choi, S. F. Xie, M. H. Shao, J. H. Odell, N. Lu, H. C. Peng, L. Protsailo, S. Guerrero, J. H. Park, X. H. Xia, J. G. Wang, M. J. Kim, Y. Xia, *Nano Lett.* **2013**, *13*, 3420.
- [18] H. Lee, S. E. Habas, S. Kweskin, D. Butcher, G. A. Somorjai, P. Yang, *Angew. Chem., Int. Ed.* **2006**, *45*, 7824.
- [19] Q. Li, L. Wu, G. Wu, D. Su, H. Lv, S. Zhang, W. Zhu, A. Casimir, H. Zhu, A. Mendoza-Garcia, S. Sun, *Nano Lett.* **2015**, *15*, 2468.
- [20] Y. Yan, J. S. Du, K. D. Gilroy, D. Yang, Y. Xia, H. Zhang, *Adv. Mater.* **2017**, *29*, 1605997.



- [21] D. Wang, H. L. Xin, R. Hovden, H. S. Wang, Y. C. Yu, D. A. Muller, F. J. DiSalvo, H. D. Abruna, *Nat. Mater.* **2013**, 12, 81.
- [22] S. Zhang, X. Zhang, G. Jiang, H. Zhu, S. Guo, D. Su, G. Lu, S. Sun, *J. Am. Chem. Soc.* **2014**, 136, 7734.
- [23] H. Zhu, S. Zhang, S. Guo, D. Su, S. Sun, *J. Am. Chem. Soc.* **2013**, 135, 7130.
- [24] V. Mazumder, M. Chi, K. L. More, S. Sun, *J. Am. Chem. Soc.* **2010**, 132, 7848.
- [25] J. Li, S. Sharma, X. Liu, Y.-T. Pan, J. S. Spendelow, M. Chi, Y. Jia, P. Zhang, D. A. Cullen, Z. Xi, H. Lin, Z. Yin, B. Shen, M. Muzzio, C. Yu, Y. S. Kim, A. A. Peterson, K. L. More, H. Zhu, S. Sun, *Joule* **2019**, 3, 124.
- [26] W. S. Jung, B. N. Popov, *ACS Appl. Mater. Interfaces* **2017**, 9, 23679.
- [27] D. Wang, Y. Yu, H. L. Xin, R. Hovden, P. Ercius, J. A. Mundy, H. Chen, J. H. Richard, D. A. Muller, F. J. DiSalvo, H. D. Abruna, *Nano Lett.* **2012**, 12, 5230.
- [28] L. Bu, N. Zhang, S. Guo, X. Zhang, J. Li, J. L. Yao, T. Wu, G. Lu, J. Y. Ma, D. Su, X. Huang, *Science* **2016**, 354, 1410.
- [29] Q. Feng, S. Zhao, D. He, S. Tian, L. Gu, X. Wen, C. Chen, Q. Peng, D. Wang, Y. Li, *J. Am. Chem. Soc.* **2018**, 140, 2773.
- [30] N. Becknell, Y. Son, D. Kim, D. Li, Y. Yu, Z. Niu, T. Lei, B. T. Sneed, K. L. More, N. M. Markovic, V. R. Stamenkovic, P. Yang, *J. Am. Chem. Soc.* **2017**, 139, 11678.
- [31] K. A. Kuttiyil, K. Sasaki, Y. M. Choi, D. Su, P. Liu, R. R. Adzic, *Nano Lett.* **2012**, 12, 6266.
- [32] C. Cui, L. Gan, H. H. Li, S. H. Yu, M. Heggen, P. Strasser, *Nano Lett.* **2012**, 12, 5885.
- [33] X. Huang, Z. Zhao, L. Cao, Y. Chen, E. Zhu, Z. Lin, M. Li, A. Yan, A. Zettl, Y. M. Wang, X. Duan, T. Mueller, Y. Huang, *Science* **2015**, 348, 1230.
- [34] W. Sun, X. Rui, D. Zhang, Y. Jiang, Z. Sun, H. Liu, S. Dou, *J. Power Sources* **2016**, 309, 135.
- [35] X. Huang, E. Zhu, Y. Chen, Y. Li, C. Chiu, Y. Xu, Z. Lin, X. Duan, Y. Huang, *Adv. Mater.* **2013**, 25, 2974.
- [36] C. Cui, L. Gan, M. Heggen, S. Rudi, P. Strasser, *Nat. Mater.* **2013**, 12, 765.
- [37] L. Zou, J. Fan, Y. Zhou, C. Wang, J. Li, Z. Zou, H. Yang, *Nano Res.* **2015**, 8, 2777.
- [38] H. Y. Kim, S. Cho, Y. J. Sa, S. M. Hwang, G. G. Park, T. J. Shin, H. Y. Jeong, S. D. Yim, S. H. Joo, *Small* **2016**, 12, 5347.
- [39] J. Kim, Y. Lee, S. Sun, *J. Am. Chem. Soc.* **2010**, 132, 4996.
- [40] M. Li, Z. Zhao, T. Cheng, A. Fortunelli, C. Y. Chen, R. Yu, Q. Zhang, L. Gu, B. V. Merinov, Z. Lin, E. Zhu, T. Yu, Q. Jia, J. Guo, L. Zhang, W. A. Goddard, Y. Huang, X. Duan, *Science* **2016**, 354, 1414.
- [41] Z. Cui, H. Chen, M. Zhao, F. J. DiSalvo, *Nano Lett.* **2016**, 16, 2560.
- [42] A. A. El-Gendy, S. Hampel, B. Buchner, R. Klingeler, *RSC Adv.* **2016**, 6, 52427.
- [43] D. Vasumathi, A. L. Shapiro, B. B. Maranville, F. Hellman, *J. Magn. Magn. Mater.* **2001**, 223, 221.
- [44] G. Kim, T. Hiratsuka, H. Naganuma, M. Oogane, Y. Ando, *J. Phys.: Conf. Ser.* **2010**, 200, 052011.
- [45] B. Zhang, Z. Zhang, H. Liao, Y. Gong, L. Gu, X. Qu, L. You, S. Liu, L. Huang, X. Tian, R. Huang, F. Zhu, T. Liu, Y. Jiang, Z. Zhou, S. Sun, *Nano Energy* **2016**, 19, 198.
- [46] J. Lim, H. Shin, M. Kim, H. Lee, K.-S. Lee, Y. Kwon, D. Song, S. Oh, H. Kim, E. Cho, *Nano Lett.* **2018**, 18, 2450.
- [47] X. Du, Y. He, X. Wang, J. Wang, *Energy Environ. Sci.* **2016**, 9, 2623.
- [48] J. Li, Z. Xi, Y.-T. Pan, J. S. Spendelow, P. N. Duchesne, D. Su, Q. Li, C. Yu, Z. Yin, B. Shen, Y. S. Kim, P. Zhang, S. Sun, *J. Am. Chem. Soc.* **2018**, 140, 2926.
- [49] Q. Liu, L. Du, G. Fu, Z. Cui, Y. Li, D. Dang, X. Gao, Q. Zheng, J. B. Goodenough, *Adv. Energy Mater.* **2019**, 9, 1803040.
- [50] N. Zhang, X. Chen, Y. Lu, L. An, X. Li, D. Xia, Z. Zhang, J. Li, *Small* **2014**, 10, 2662.
- [51] N. Cheng, L. Zhang, S. Mi, H. Jiang, Y. Hu, H. Jiang, C. Li, *ACS Appl. Mater. Interfaces* **2018**, 10, 38015.
- [52] H. Zhu, S. Zhang, D. Su, G. Jiang, S. Sun, *Small* **2015**, 11, 3545.
- [53] V. T. Ho, C. J. Pan, J. Rick, W. N. Su, B. J. Hwang, *J. Am. Chem. Soc.* **2011**, 133, 11716.
- [54] J. Zhang, K. Sasaki, E. Sutter, R. R. Adzic, *Science* **2007**, 315, 220.
- [55] P. Strasser, S. Koh, T. Anniyev, J. Greeley, K. More, C. Yu, Z. Liu, S. Kaya, D. Nordlund, H. Ogasawara, M. F. Toney, A. Nilsson, *Nat. Chem.* **2010**, 2, 454.
- [56] M. Luo, S. Guo, *Nat. Rev. Mater.* **2017**, 2, 17059.
- [57] J. K. Nørskov, J. Rossmeisl, A. Logadottir, L. Lindqvist, J. R. Kitchin, T. Bligaard, H. Jónsson, *J. Phys. Chem. B* **2004**, 108, 17886.
- [58] V. Stamenkovic, B. S. Mun, K. J. Mayrhofer, P. N. Ross, N. M. Markovic, J. Rossmeisl, J. Greeley, J. K. Nørskov, *Angew. Chem., Int. Ed.* **2006**, 45, 2897.
- [59] X. W. Zhou, R. A. Johnson, H. N. G. Wadley, *Phys. Rev. B* **2004**, 69, 144113.
- [60] J. K. Nørskov, J. Rossmeisl, A. Logadottir, L. Lindqvist, J. R. Kitchin, T. Bligaard, H. Jónsson, *J. Phys. Chem. B* **2004**, 108, 17886.
- [61] Z. Chen, X. Zhang, G. Lu, *Chem. Sci.* **2015**, 6, 6829.